

ACCEPTED MANUSCRIPT • OPEN ACCESS

Overview of first Wendelstein 7-X high-performance operation

To cite this article before publication: Thomas Klinger *et al* 2019 *Nucl. Fusion* in press <https://doi.org/10.1088/1741-4326/ab03a7>

Manuscript version: Accepted Manuscript

Accepted Manuscript is “the version of the article accepted for publication including all changes made as a result of the peer review process, and which may also include the addition to the article by IOP Publishing of a header, an article ID, a cover sheet and/or an ‘Accepted Manuscript’ watermark, but excluding any other editing, typesetting or other changes made by IOP Publishing and/or its licensors”

This Accepted Manuscript is © EURATOM 2019.

As the Version of Record of this article is going to be / has been published on a gold open access basis under a CC BY 3.0 licence, this Accepted Manuscript is available for reuse under a CC BY 3.0 licence immediately.

Everyone is permitted to use all or part of the original content in this article, provided that they adhere to all the terms of the licence
<https://creativecommons.org/licenses/by/3.0>

Although reasonable endeavours have been taken to obtain all necessary permissions from third parties to include their copyrighted content within this article, their full citation and copyright line may not be present in this Accepted Manuscript version. Before using any content from this article, please refer to the Version of Record on IOPscience once published for full citation and copyright details, as permissions may be required. All third party content is fully copyright protected and is not published on a gold open access basis under a CC BY licence, unless that is specifically stated in the figure caption in the Version of Record.

View the [article online](#) for updates and enhancements.

Overview of first Wendelstein 7-X high-performance operation

T. Klinger^{1,2}, T. Andreeva¹, S. Bozhenkov¹, C. Brandt¹, R. Burhenn¹, B. Buttenschön¹, G. Fuchert¹, B. Geiger¹, O. Grulke^{1,3}, H.P. Laqua¹, N. Pablant⁴, K. Rahbarnia¹, T. Stange¹, A. von Stechow¹, N. Tamura⁵, H. Thomsen¹, Y. Turkin¹, T. Wegner¹, I. Abramovic¹, S. Äkäslompolo¹, J. Alcusion¹, P. Aleynikov¹, K. Aleynikova¹, A. Ali¹, A. Alonso⁶, G. Anda⁷, E. Ascasibar⁶, J. P. Bähner¹, S. G. Baek⁹, M. Balden¹⁰, J. Baldzuhn¹, M. Banduch¹, T. Barbui¹¹, W. Behr⁸, C. Beidler¹, A. Benndorf¹, C. Biedermann¹, W. Biel⁸, B. Blackwell¹², E. Blanco⁶, M. Blatzheim¹, S. Ballinger⁹, T. Bluhm¹, D. Böckenhoff¹, B. Böswirth¹⁰, L.-G. Böttger^{1,3}, M. Borchardt¹, V. Borsuk⁸, J. Boscary¹⁰, H.-S. Bosch¹, M. Beurskens¹, R. Brakel¹, H. Brand¹³, T. Bräuer¹, H. Braune¹, S. Brezinsek⁸, K.-J. Brunner¹, R. Bussiahn¹, V. Bykov¹, J. Cai⁸, I. Calvo⁶, B. Cannas¹⁴, A. Cappa⁶, A. Carls¹, D. Carralero⁶, L. Carraro¹⁵, B. Carvalho¹⁶, F. Castejon⁶, A. Charl⁸, N. Chaudhary¹, D. Chauvin¹⁷, F. Chernyshev¹⁸, M. Cianciosa¹⁹, R. Citarella²⁰, G. Claps²¹, J. Coenen⁸, M. Cole¹, M.J. Cole¹⁹, F. Cordella²¹, G. Cseh⁷, A. Czarnecka²², K. Czerski²³, M. Czerwinski¹, G. Czymek⁸, A. da Molin²⁴, A. da Silva¹⁷, H. Damm¹, A. de la Pena⁶, S. Degenkolbe¹, C. P. Dhard¹, M. Dibon¹⁰, A. Dinklage¹, T. Dittmar⁸, M. Drevlak¹, P. Drewelow¹, P. Drews⁸, F. Durodie²⁶, E. Edlund⁹, P. van Eeten¹, F. Effenberg¹¹, G. Ehrke¹, S. Elgeti¹⁰, M. Endler¹, D. Ennis²⁷, H. Esteban⁶, T. Estrada⁶, J. Fellinger¹, Y. Feng¹, E. Flom¹¹, H. Fernandes¹⁷, W. H. Fietz²⁵, W. Figacz²², J. Fontdecaba⁶, O. Ford¹, T. Fornal²², H. Frerichs¹⁰, A. Freund⁸, T. Funaba⁵, A. Galkowski²², G. Gantenbein²⁵, Y. Gao⁸, J. García Regaña⁶, D. Gates⁴, J. Geiger¹, V. Giannella²⁰, A. Gogoleva²⁸, B. Goncalves¹⁷, A. Goriaev²⁶, D. Gradic¹, M. Grahl¹, J. Green¹¹, H. Greuner¹⁰, A. Grosman¹⁷, H. Grote¹, M. Gruca²², C. Guerard⁶, P. Hacker¹, X. Han⁸, J.H. Harris¹⁹, D. Hartmann¹, D. Hathiramani¹, B. Hein¹, B. Heinemann¹⁰, P. Helander^{1,2}, S. Henneberg¹, M. Henkel⁸, J. Hernandez Sanchez⁶, C. Hidalgo⁶, M. Hirsch¹, K.P. Hollfeld⁸, U. Höfel¹, A. Höltинг¹, D. Höschen⁸, M. Houry¹⁷, J. Howard¹³,

1
2 *Overview of first Wendelstein 7-X high-performance operation*

3
4 X. Huang⁵, Z. Huang¹, M. Hubeny⁸, M. Huber²⁵, H. Hunger²⁵,
5 K. Ida⁵, T. Ilkei⁷, S. Illy²⁵, B. Israeli⁴, S. Jablonski²², M.
6 Jakubowski¹, J. Jelonnek²⁵, H. Jenzsch¹, T. Jesche²⁹, M. Jia⁸,
7 P. Junghanns¹⁰, J. Kacmarczyk²², J.-P. Kallmeyer¹, U.
8 Kamionka¹, H. Kasahara⁵, W. Kasperek²⁹, Y. O. Kazakov²⁶, N.
9 Kenmochi⁵, C. Killer¹, A. Kirschner⁸, R. Kleiber¹, J. Knauer¹,
10 M. Knaup⁸, A. Knieps⁸, T. Kobarg²⁵, G. Kocsis⁷, F. Köchl³⁰, Y.
11 Kolesnichenko³¹, A. Könies¹, R. König¹, P. Kornejew¹, J.-P.
12 Koschinsky¹, F. Köster³², M. Krämer²⁹, R. Krampitz¹, A.
13 Krämer-Flecken⁸, N. Krawczyk²², T. Kremeyer¹¹, J. Krom¹, M.
14 Krychowiak¹, I. Ksiazek³³, M. Kubkowska²², G. Kühner¹, T.
15 Kurki-Suonio³⁴, P. A. Kurz¹, S. Kwak¹, M. Landreman³⁵, P.
16 Lang¹⁰, R. Lang²⁵, A. Langenberg¹, S. Langish⁴, H. Laqua¹, R.
17 Laube¹, S. Lazerson⁴, C. Lechte²⁹, M. Lennartz⁸, W.
18 Leonhardt²⁵, C. Li¹, C. Li⁸, Y. Li⁸, Y. Liang⁸, C. Linsmeier⁸, S.
19 Liu⁸, J.-F. Lobsien¹, D. Loesser⁶, J. Loizu Cisquella¹, J. Lore¹⁹,
20 A. Lorenz¹, M. Losert²⁵, A. Lücke⁴⁵, A. Lumsdaine¹⁹, V.
21 Lutsenko³¹, H. Maßberg¹, O. Marchuk⁸, J. H. Matthew¹², S.
22 Marsen¹, M. Marushchenko¹, S. Masuzaki⁵, D. Maurer²⁷, M.
23 Mayer¹⁰, K. McCarthy⁶, P. McNeely¹, A. Meier²⁵, D. Mellein²⁵,
24 B. Mendelevitch¹⁰, P. Mertens⁸, D. Mikkelsen⁴, A.
25 Mishchenko¹, B. Missal¹, J. Mittelstaedt⁴, T. Mizuuchi⁴⁶, A.
26 Mollen¹, V. Moncada¹⁷, T. Mönnich¹, T. Morisaki⁵, D.
27 Moseev¹, S. Murakami⁴⁶, G. Náfrádi⁷, M. Nagel¹, D. Naujoks¹,
28 H. Neilson⁴, R. Neu¹⁰, O. Neubauer⁸, U. Neuner¹, T. Ngo¹⁷, D.
29 Nicolai⁸, S. K Nielsen³, H. Niemann¹, T. Nishizawa¹, R.
30 Nocentini¹⁰, C. Nührenberg¹, J. Nührenberg¹, S. Obermayer¹⁰,
31 G. Offermanns⁸, K. Ogawa⁵, J. Ölmanns⁸, J. Ongena²⁶, J.W.
32 Oosterbeek¹, G. Orozco¹⁰, M. Otte¹, L. Pacios Rodriguez⁶, N.
33 Panadero¹, N. Panadero Alvarez⁶, D. Papenfuß²⁵, S. Paqay¹³,
34 E. Pasch¹, A. Pavone¹, E. Pawelec³³, T. S. Pedersen^{1,2}, G.
35 Pelka²², V. Perseo¹, B. Peterson⁵, D. Pilopp¹, S. Pingel¹, F.
36 Pisano¹⁴, B. Plaum²⁹, G. Plunk¹, P. Pölöskei¹⁰, M. Porkolab⁹, J.
37 Proll¹³, M.-E. Puiatti³⁶, A. Puig Sitjes¹, F. Purps¹, M. Rack⁸,
38 S. Récsyi⁷, A. Reiman⁴, F. Reimold¹, D. Reiter⁸, F. Remppel²⁹,
39 S. Renard¹⁷, R. Riedl¹⁰, J. Riemann¹, K. Risse¹, V. Rohde¹⁰, H.
40 Röhlinger²⁹, M. Romé³⁶, D. Rondeshagen¹, P. Rong¹, B.
41 Roth²⁹, L. Rudischhauser¹, K. Rummel¹, T. Rummel¹, A.
42 Runov¹, N. Rust¹, L. Ryc²², S. Ryosuke⁵, R. Sakamoto⁵, M.
43 Salewski³, A. Samartsev²⁵, E. Sanchez⁶, F. Sano³⁷, S. Satake⁵,
44 J. Schacht¹, G. Satheeswaran⁸, F. Schauer¹, T. Scherer²⁵, J.
45 Schilling¹, A. Schlaich²⁵, G. Schlisio¹, F. Schluck⁸, K.-H.

1
2 *Overview of first Wendelstein 7-X high-performance operation* 3
3
4
5 Schlüter²⁹, J. Schmitt²⁷, H. Schmitz⁸, O. Schmitz¹⁰, S.
6 Schmuck³⁸, M. Schneider¹, W. Schneider¹, P. Scholz¹, R.
7 Schrittwieser³⁰, M. Schröder¹, T. Schröder¹, R. Schroeder¹, H.
8 Schumacher³⁹, B. Schweer²⁶, E. Scott¹, S. Sereda⁸, B.
9 Shanahan¹, M. Sibilia⁴, P. Sinha¹, S. Sippliä³⁴, C. Slaby¹, M.
10 Sleczka²³, H. Smith¹, W. Spiess²⁵, D.A. Spong¹⁹, A. Spring¹, R.
11 Stadler¹⁰, M. Stejner³, L. Stephey¹¹, U. Stridde⁴, C. Suzuki⁵, J.
12 Svensson¹, V. Szabó⁷, T. Szabolics⁷, T. Szepesi⁷, Z.
13 Szökefalvi-Nagy⁷, A. Tancetti³, J. Terry⁹, J. Thomas⁸, M.
14 Thumm²⁵, J. M. Travere¹⁷, P. Traverso²⁷, J. Tretter¹⁰, H.
15 Trimino Mora¹, H. Tsuchiya⁵, T. Tsujimura⁵, S. Tulipán⁷, B.
16 Unterberg⁸, I. Vakulchyk¹, S. Valet¹, L. Vano⁷, B. van
17 Milligen⁶, A. J. van Vuuren¹⁰, L. Vela²⁸, J.-L. Velasco⁶, M.
18 Vergote²⁶, M. Vervier²⁶, N. Vianello⁵³, H. Viebke¹, R.
19 Vilbrandt¹, A. Vorköper¹, S. Wadle²⁵, F. Wagner¹, E. Wang⁸,
20 N. Wang⁸, Z. Wang¹, F. Warmer¹, T. Wauters²⁶, L. Wegener¹,
21 J. Weggen²⁵, Y. Wei⁸, G. Weir¹, J. Wendorf¹, U. Wenzel¹, A.
22 Werner¹, A. White⁹, B. Wiegel⁴⁵, F. Wilde¹, T. Windisch¹, M.
23 Winkler¹, A. Winter¹, V. Winters¹¹, S. Wolf²⁹, R.C. Wolf^{1,32}, A.
24 Wright¹², G. Wurden⁴⁰, P. Xanthopoulos¹, H. Yamada⁵, I.
25 Yamada⁵, R. Yasuhara⁵, M. Yokoyama⁵, M. Zanini¹, M.
26 Zarnstorff⁴, A. Zeitler²⁹, D. Zhang¹, H. Zhang⁶, J. Zhu¹, M.
27 Zilker¹⁰, A. Zocco¹, S. Zoleznik⁷ and M. Zuin¹³

35 ¹ Max-Planck Institute for Plasma Physics, Wendelsteinstrasse 1, 17491 Greifswald,
36 Germany

37 ² Greifswald University, Domstrasse 11, 17489 Greifswald, Germany

38 ³ Technical University of Denmark, Anker Engelunds Vej 1, 2800 Kgs. Lyngby,
39 Denmark

40 ⁴ Princeton Plasma Physics Laboratory, 100 Stellarator Rd, Princeton, NJ 08540,
41 United States of America

42 ⁵ National Institute for Fusion Science, 322-6 Ooshicho, Toki, Gifu Prefecture
43 509-5202, Japan

44 ⁶ CIEMAT, Avenida Complutense, 40, 28040 Madrid, Spain

45 ⁷ Wigner Research Centre for Physics, Konkoly Thege Miklos ut 29-33, 1121
46 Budapest, Hungary

47 ⁸ Research Center Jülich GmbH, Institute for Energy and Climate Research Plasma
48 Physics, Wilhelm-Johnen-Strasse, 52428 Jülich, Germany

49 ⁹ Massachusetts Institute of Technology, 77 Massachusetts Ave, Cambridge, MA
50 02139, United States of America

51 ¹⁰ Max-Planck Institute for Plasma Physics, Boltzmannstrasse 2, 85748 Garching,
52 Germany

53 ¹¹ University of Wisconsin Madison, Engineering Drive, Madison, WI 53706, United
54 States of America

55 ¹² The Australian National University, Acton ACT 2601, Canberra, Australia

56 ¹³ Eindhoven University of Technology, 5612 AZ Eindhoven, Netherlands

57 ¹⁴ University of Cagliari, Via Universita, 40, 09124 Cagliari, Italy

1 2 Overview of first Wendelstein 7-X high-performance operation 3 4

5

5 transiently accomplished, which corresponds to $nT_i(0)\tau_E = 6.4 \cdot 10^{19} \text{ keVs/m}^3$ with a
6 peak diamagnetic energy of 1.1 MJ and volume-averaged normalized plasma pressure
7 $\langle\beta\rangle = 1.2\%$. The routine access to high plasma densities was opened with boronization
8 of the first wall. After boronization, the oxygen impurity content was reduced by a
9 factor of 10, the carbon impurity content by a factor of 5. The reduced (edge) plasma
10 radiation level gives routinely access to higher densities without radiation collapse,
11 e.g. well above $1 \times 10^{20} \text{ m}^{-2}$ line integrated density and $T_e = T_i = 2 \text{ keV}$ central
12 temperatures at moderate ECRH power. Both X2 and O2 mode ECRH schemes were
13 successfully applied. Core turbulence was measured with a phase contrast imaging
14 diagnostic and suppression of turbulence during pellet injection was observed.
15
16

17 PACS numbers: 00.00, 20.00, 42.10
18
19

20 Submitted to: *Nucl. Fusion*
21
22

1. Introduction

25 Stellarators are free from current disruptions and are intrinsically capable to sustain a
26 plasma steady-state without need for current drive [1]. The stellarator magnetic field,
27 however, needs to be optimized to overcome major issues in neoclassical transport,
28 magnetohydrodynamic equilibrium and stability, and fast particle confinement, in
29 particular at high plasma beta and low collisionality [2, 3, 4]. After successful first
30 operation [5, 6, 7], the optimized stellarator device Wendelstein 7-X [8, 9] is now
31 operating with (yet uncooled) graphite heat shields and a graphite island divertor
32 [10, 11]. Wendelstein 7-X is a high-iota, low shear stellarator with optimized magnetic
33 field geometry and 30 m^3 plasma volume. It is the mission of the device to demonstrate
34 steady-state (pulse length $T_p \leq 1800 \text{ s}$) generation and confinement of fusion-relevant
35 hydrogen and deuterium plasmas. The magnetic field with induction 2.5 T on the
36 magnetic axis is generated using a set of non-planar and planar liquid-helium cooled
37 superconducting NbTi coils. All plasma facing components are designed for active
38 water cooling capability. Steady-state electron cyclotron resonance plasma heating is
39 provided by long-pulse gyrotrons. Neutral beam injectors and ion cyclotron resonance
40 heating are foreseen for high beta plasmas and fast particle physics investigations.
41
42

43 The device operation phase reported in the present paper is performed without
44 water cooling of the main in-vessel components. This restricts the heating energy input
45 to 200 MJ. High-performance plasma operation is nevertheless possible, but at limited
46 pulse lengths (typical 10 – 30 s). Long discharges (up to 100 s) are restricted to lower
47 heating power and consequently lower plasma performance. Fully integrated divertor
48 operation must be demonstrated to develop a basis for high-performance steady-state
49 operation which follows after the completion of the cooling water systems and the
50 installation of the water-cooled divertor and the cryo pumps.
51
52

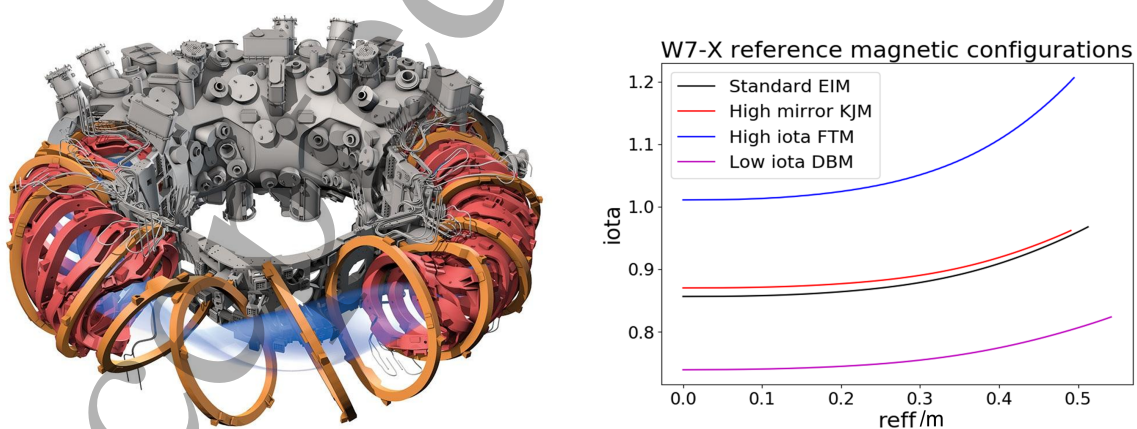
53 The present paper is structured in a machine description Sec. 2, long-pulse high
54 density plasmas Sec. 3, and stellarator optimization Sec. 4. The paper is summarized
55 in Sec. 5.
56
57

1
2 *Overview of first Wendelstein 7-X high-performance operation*
3
4
5
6

2. The Wendelstein 7-X stellarator device

7 As pointed out in Sec. 1, the magnetic field geometry of the superconducting stellarator
8 Wendelstein 7-X was optimized to address major issues of the classical stellarator [3, 4].
9 A schematic drawing of the device and the rotational transform of some of the magnetic
10 field configurations are shown in Fig.1. The 50 non-planar coils (red) and 20 planar coils
11 (orange) are connected in series via superconducting bus bars. All coils are bolted to a
12 massive central support ring (gray) and additionally fixed by mostly welded, partially
13 bolted or sliding local support elements. The complete magnet system and the support
14 structures are cooled down to 3.4 K in the cryostat vacuum between the outer vessel
15 and the plasma vessel. Both the plasma vessel, the outer vessel and the 253 ports are
16 covered with a thermal insulation, based on multi-layer foil and a thermal shield actively
17 cooled to 70 K [12].
18
19

20 The main device parameters are listed in Tab. 1. Stage 1 was the setup for the
21 initial operation. After substantial extension of the in-vessel components and the heating
22 systems, the present stage 2 was reached. Stage 3 is planned for the subsequent operation
23 phase. Stage 4 is the projected full performance configuration of the device. The most
24 powerful heating scheme of Wendelstein 7-X is the electron cyclotron resonance heating
25 (ECRH) with at present 10 long-pulse capable 140 GHz gyrotrons [13]. On average each
26 gyrotron accounts for 0.8 MW power coupled into the plasma which provides a highly
27 flexible X2-mode and O2-mode heating scheme, both on- and off-axis. The flexibility and
28 the well-defined heat deposition in the electron cyclotron resonance zone render ECRH
29 being the most advanced heating and current drive scheme with the biggest potential for
30
31
32
33
34



52 **Figure 1.** Schematic diagram of the superconducting stellarator device Wendelstein
53 7-X. The last closed magnetic flux surface is indicated in light blue. The 50 non-planar (red)
54 and the 20 planar (orange) superconducting coils are operated in a evacuated
55 cryostat volume between the plasma vessel and the outer vessel. Wendelstein 7-X is
56 a high-iota low-shear device and the iota profiles ($\beta = 0$) of some reference magnetic
57 configurations are shown on the right hand side. The reference configurations are
58 standard (EIM), high mirror ratio (KJM), high iota (FTM), and low iota (DBM).
59
60

1
2 *Overview of first Wendelstein 7-X high-performance operation*
3
4
5
6
7
8

5 **Table 1.** Major parameters of the stellarator Wendelstein 7-X. The different stages of
6 completion and extension mainly determine the available heating power and the active
7 cooling of the in-vessel components.
8

9 quantity	10 unit	11 stage 1	12 stage 2	13 stage 3	14 stage 4
11 plasma volume	12 m ²			30	
12 major radius	13 m			5.5	
13 minor radius	14 m			0.5	
14 magnetic induction on axis	15 T			2.5	
15 rotational transform	16 2π			5/6...5/4	
16 ECR heating power	17 MW	4.3	8.5	10	10-15
17 ICR heating power	18 MW			1.5	3.5
18 NBI heating power H/D	19 MW		3.5	7/10	14/20
19 heating energy	20 MJ	4	200	1000	18000
20 pulse length typ.	21 s	1-2	10-100	100-200	100-1800

25
26
27 a future stellarator power reactor [14]. The first of two neutral beam injector (NBI) boxes
28 have started operation with two positive ion sources and 55 kV acceleration voltage and
29 up to 3.5 MW injection power [15]. The ion cyclotron resonance heating (ICRH) system
30 requires an antenna that is carefully shaped to the three-dimensional plasma contour.
31 This development is ongoing and commissioning is foreseen for the next operation phase
32 [16]. To protect the (mostly uncooled) in-vessel components, the maximum heating
33 energy during stage 2 is at present limited to 200 MJ, which implies typical discharge
34 times between 10 and 100 s, depending on the input power. After completion of the
35 water cooling systems and the replacement of the inertially cooled island divertor with
36 an actively water-cooled one, the maximum heating energy will be extended step-wise
37 to 18 GJ with at least one intermediate step at 1 GJ (stage 3).
38
39
40
41

42 Wendelstein 7-X started first operation in the year 2015. The heat and particle
43 exhaust was controlled with five poloidal graphite limiters, the remaining wall was either
44 steel or CuCrZr. Despite the unfavorable wall conditions, the plasma performance was
45 quite remarkable with peak electron temperatures 8 keV with simultaneous peak ion
46 temperature 2 keV and line averaged density $3 \times 10^{19} \text{ m}^{-3}$ [5, 6, 7]. These are typical
47 conditions for the core electron root confinement [5, 6, 7, 17] which is characterized by
48 a reversal of the radial electric field from edge to core [18]. First elements of stellarator
49 optimization could be demonstrated by studying the bootstrap current and neoclassical
50 transport [19].
51
52

53
54 For the second operation phase (stage 2) the limiters were replaced by an island
55 divertor and major areas of the wall are covered with graphite tiles. The island divertor
56 consists of ten separate modules formed by graphite target and baffle plates that are
57 matched to the magnetic field structure of Wendelstein 7-X [10, 11]. Depending on
58 the magnetic configuration (given by the rotational transform $\iota/2\pi$, cf. Fig. 1) natural
59
60

1
2 *Overview of first Wendelstein 7-X high-performance operation*
3
4
5
6
7
8
9

10
11
12
13 **Table 2.** Total surface and maximum allowable heat flux of the in-vessel components
14 of Wendelstein 7-X. The graphite divertor targets are presently replaced with carbon-
15 fibre reinforced carbon targets* (stage 3). All in-vessel components are pressure water-
16 cooled from the next operation phase onwards.
17
18
19
20
21

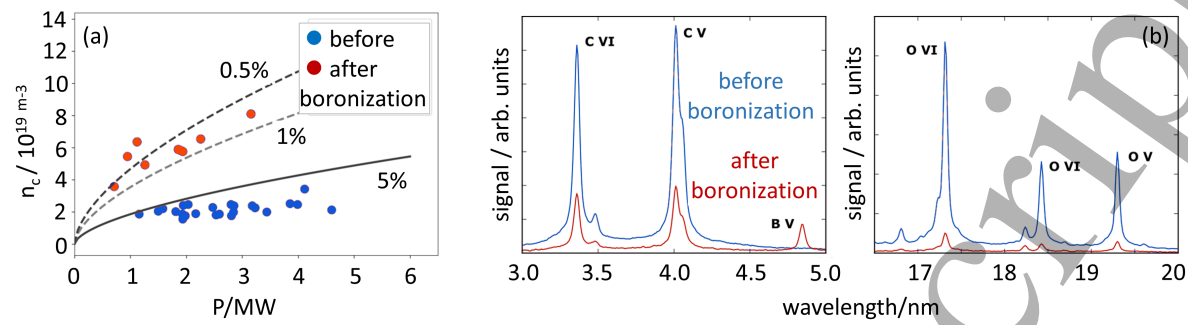
in-vessel element	material	surface/m ²	heat flux/MW/m ²
		total	maximum
divertor targets	graphite/CFC*	19	10
divertor baffles	graphite	22	0.5
divertor closures	steel	10	0.2
heat shield	graphite	47	0.3
panels	steel	62	0.2
port liners	steel	~ 100	0.2

22
23 magnetic islands form at the plasma boundary. They are intersected with the divertor
24 target plates and thus establish a multi-X-point divertor for the exhaust of particle and
25 heat flows across the last closed flux surface. The aim of the second operation phase
26 is to demonstrate full divertor operation and exhaust combined with improved plasma
27 performance.
28
29

30
31 **3. High density stationary discharges**
32
33

34 The plasma performance of Wendelstein 7-X in terms of plasma density, ion temperature,
35 stored energy, and discharge duration has dramatically improved after the installation
36 of the graphite heat shields and the graphite island divertor. Another significant step
37 forward was made with a suite of wall conditioning measures [20]: The plasma vessel
38 is baked at 150 deg C in order to remove water and hydrocarbons from the vessel wall
39 and in-vessel components. Without magnetic field, glow discharge cleaning (GDC)
40 is applied in hydrogen (to reduce residual CO and CH₄) and helium gas (to reduce
41 H₂). With the superconducting magnets ramped up, an additional wall conditioning
42 inbetween discharges was made with ECRH short pulse trains followed by pumping
43 intervals. The GDC in helium and hydrogen as well as the occasional ECRH pulse train
44 conditioning of the plasma facing components (with total surface areas of 88 m² graphite
45 and 82 m² steel) have greatly reduced the outgassing rates, rapidly dropping to values
46 that were reached only at the end of the initial (stage 1) operation phase with graphite
47 limiters. Plasma densities of 1 – 5 × 10¹⁹ m⁻³ with electron temperature 5 – 10 keV
48 were achieved with hydrogen gas fueling; higher densities where not accessible due to
49 the radiative limit. High plasma densities up to 1.4 × 10²⁰ m⁻³ could be reached with
50 repetitive hydrogen pellet injection and second harmonic ECR heating in O-polarization
51 (O2-scheme, cf. Fig 3(b) below). In a similar scenario with hydrogen plasma, at a
52 central density of 8 × 10¹⁹ m⁻³, the ions are indirectly heated and a temperature of
53
54
55
56
57
58
59
60

1
2 Overview of first Wendelstein 7-X high-performance operation
3
4

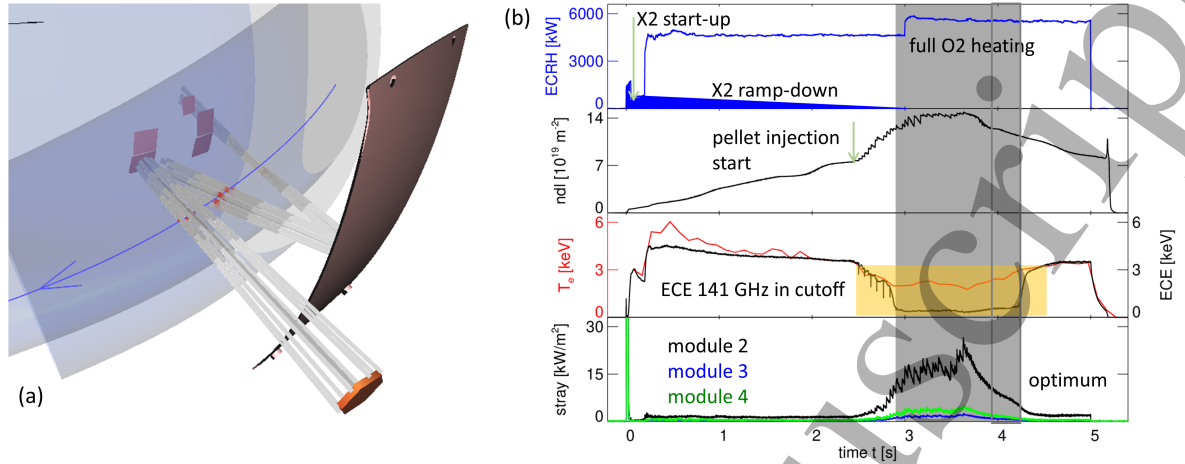


15
16 **Figure 2.** (a) Maximum density achieved before onset of radiation collapse versus
17 heating power before (blue symbols) and after boronization (red symbols). The lines
18 indicate the predicted critical density n_c for different impurity fractions $f_{\text{imp}} = 5\%$, 1%
19 and 0.5% . (b) Spectral lines of C and O ionization stages before and after boronization.
20 At about 4.9 nm a small B V line arises after boronization.
21
22

23 3.4 keV with $T_e/T_i \approx 1$ was accomplished, still with second harmonic ECR heating
24 in X-polarization (X2-scheme). This discharge corresponds to a (stellarator) record
25 $nT_i(0)\tau_E = 6.4 \times 10^{19} \text{ keVs/m}^3$ with a peak diamagnetic energy of 1.1 MJ and volume-
26 averaged normalized plasma pressure $\langle\beta\rangle = 1.5\%$ [21, 22]. The corresponding radial
27 temperature and density profiles are both centrally peaked with typical gradient lengths
28 $L_{T_{e,i}} \approx 3 - 4 \text{ m}$ and $L_n \approx 2 - 3 \text{ m}$. The radial density profile significantly steepens with
29 central fueling, e.g. by pellet injection or neutral beam injection (see below). Further
30 details about the kinetic profiles are found in Ref. [21]. Routinely, stable 25 s long-
31 pulse helium discharges with 2 – 3 MW ECRH power and up to 75 MJ injected energy
32 were created for equilibrium and divertor load studies, with plasma densities around
33 $5 \times 10^{19} \text{ m}^{-3}$ and 5 keV electron temperature.
34
35

36 Boronization was conducted for the first time half-way the experimental campaign
37 [23] (in total three times). Here, a glow discharge with 10% diborane B_2H_6 in 90% helium
38 background gas was operated for 4 – 5 hours to deposit a boron layer of about 50 – 100 nm
39 thickness. The boron layer turned out to last for at about 200 plasma seconds on the
40 strike line position of the divertor targets and for at least about 2000 plasma seconds on
41 other wall elements. In fact, the excellent wall conditions did not degrade significantly
42 during the accumulated 2400 s of plasma duration between each two boronization cycles
43 and it can be assumed that longer cycle times are well possible. Fig. 2(a) shows the
44 difference between the discharge conditions before and after boronization [24]. With
45 the same ECR heating power and normal gas puffing, about $\times 3$ higher plasma densities
46 could be reached without radiative collapse. This improvement is due to a reduced O
47 and C content, which strongly reduces the radiative power losses predominantly in the
48 plasma edge, where the radiative collapse usually starts. The observed critical densities
49 and their scaling with heating power is compared to the scaling law derived in Ref. [25].
50 For the Wendelstein 7-X parameters the scaling $\bar{n}_c \propto P^{0.6}/f_{\text{imp}}^{0.4}$ is plotted for different
51 impurity fraction values $f_{\text{imp}} = n_{\text{imp}}/n_e = 5\%$, 1% and 0.5% , respectively. Before
52 boronization the observed n_c values scale weaker than predicted even for $f_{\text{imp}} = 5\%$.
53
54
55
56
57
58
59
60

1
2 *Overview of first Wendelstein 7-X high-performance operation*
3
4
5
6
7
8
9
10
11
12
13
14
15
16
17
18
19
20



21 **Figure 3.** (a) Multi-pass absorption scheme using tungsten reflector tiles with
22 holographic grating, mounted on the inner and the outer sides of the in-vessel system.
23 (b) O2-mode heating scenario showing from top to bottom the heating power in
24 X- and O-mode polarization (blue), the line-integrated density, the electron density
25 measured by Thomson scattering (red) and electron cyclotron emission (black), and
26 stray radiation measured in the device module where the wave launcher is located
27 (black) and in the two neighboring modules (green and blue).

28
29
30 After boronization, there is a good agreement with the scaling law for $f_{\text{imp}} = 0.5\text{--}1\%$. To
31 highlight the effect of boronization on O and C impurities, spectroscopic measurements
32 of O V and O VI as well as C V and C VI ions before and after boronization are shown in
33 Fig. 2(b). The spectroscopic signals are normalized to the line-averaged plasma density
34 measured for the respective discharge. Note that for the lower wavelengths, no absolute
35 calibration is available and temperature and profile effects have not yet been taken
36 into account. Nevertheless, a strong reduction of the spectral line strength by $\times 2.5$ for
37 carbon and $\times 6.5\ldots 8$ for oxygen is evident and a similar reduction in the associated
38 impurity concentration can be assumed. This is a clear indication for the expected
39 gettering effect by the boron layer on the plasma facing components [26].
40
41
42

43 With the extension of the density limit, ECR heating schemes beyond the X-mode
44 cut-off density $1.2 \times 10^{20} \text{ m}^{-3}$ became important. In O-mode polarization ECR waves
45 have a cut-off density of $2.4 \times 10^{20} \text{ m}^{-3}$, with the drawback of relatively low absorption
46 rate of 70%, even at the favorable high electron temperature $T_e \simeq 3 \text{ keV}$ and density
47 $n_e = 1 \times 10^{20} \text{ m}^{-3}$. In combination with pellet injection, the heating scenario shown
48 in Fig. 3 was developed [27, 28, 29]: The plasma start-up (here in helium) is made
49 with three gyrotrons in X-mode polarization. During the following 2 s the polarization
50 is changed to O-mode polarization. At $t = 2 \text{ s}$ the density ramp-up is steepened by
51 repetitive hydrogen ice pellet injection and at $t = 3 \text{ s}$ further six gyrotrons (in O-mode)
52 are added. At the peak density of $1.4 \times 10^{20} \text{ m}^{-3}$ the electron temperature is still close
53 to 3 keV. The 141 GHz electron cyclotron emission (ECE) signal vanishes due to excess
54 of the X2-mode cut-off density (indicated by the orange strip). The stray radiation
55
56
57
58
59
60

1
2 Overview of first Wendelstein 7-X high-performance operation 11
3
4
5
6
7
8
9
10
11
12
13
14
15
16
17
18
19
20
21
22
23
24
25
26
27
28
29
30
31
32
33
34
35
36
37
38
39
40
41
42
43
44
45
46
47
48
49
50
51
52
53
54
55
56
57
58
59
60

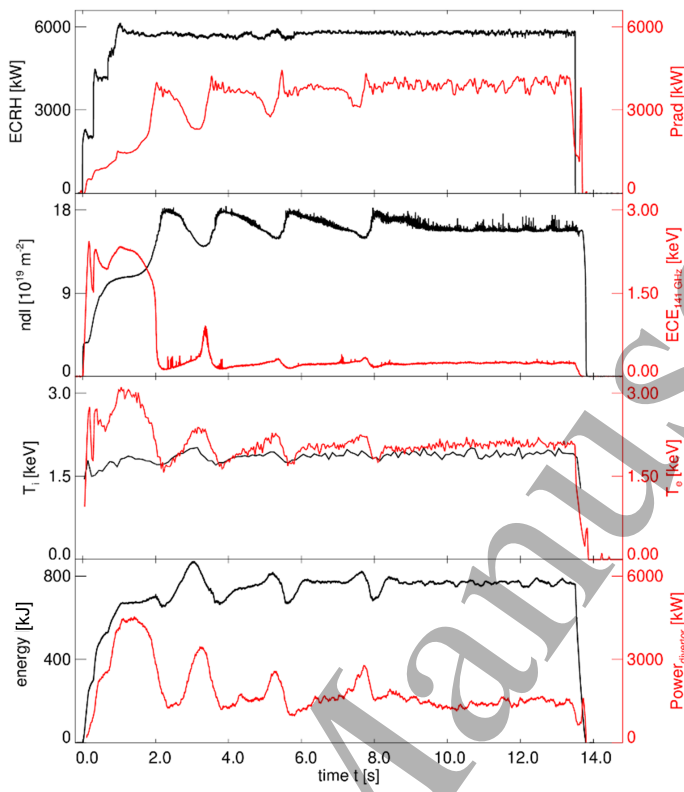


Figure 4. O2-mode heated long pulse high density plasma discharge. Shown are (from top to bottom, left and right scale) heating power, total radiative power, line-integrated density, electron cyclotron emission at 141 GHz, ion and electron temperature, diamagnetic energy and total divertor power load. The slow oscillations are generated by the feedback-controller. The 141GHz ECE channel runs into the cut-off after 2 s verifying the pure 140 GHz O2-heating.

signal always remains in an acceptable range, even in the device module where the wave launcher is located. In the optimum O2-heating regime, the stray radiation level is found to be below 10 kW/m^2 .

As outlined above, wall boronization has greatly extended the plasma density range to much higher values. After the first successful experiments in helium plasmas combined with hydrogen pellet injection, the previously described ECR O2-heating scheme became also the reference heating scheme for high density gas fueled hydrogen plasmas as well [27, 28, 29]. An example is shown in Fig. 4. The ECR heating power is 6 MW in total and is almost fully absorbed. The radiation fraction stays constant at 60%. At the (line-integrated) plasma densities $> 1 \times 10^{20} \text{ m}^{-3}$ ions are efficiently heated by the electrons and one obtains almost thermal equilibration $T_e \approx T_i$. The divertor is fully detached [30] and the power load drops to $\leq 1.5 \text{ MW}$. The discharge duration was limited to 14 s due to the technical limit of 80 MJ maximum injected energy set at that time period of operation. Since the divertor power detachment turned out to be well under control and the power load on the targets correspondingly low, the technical limit for the total heating energy could be extended from 80 to 200 MJ. A similar O2-heated

1
2 *Overview of first Wendelstein 7-X high-performance operation* 12
3
4
5
6
7
8
9
10
11
12
13
14
15
16
17

discharge could be extended to 30 s discharge duration at 5 MW heating power, again with full power detachment and similar plasma parameters [27]. In addition, high density operation could be demonstrated with pure neutral beam injection heating (3.5 MW H^+) after starting the plasma with ECRH (X2-mode). Possibly explained by the additional central fuelling from the neutral beam, the plasma density increases throughout the NBI phase with more peaked density profiles and up to $n(0) = 2 \times 10^{20} \text{ m}^{-3}$. The ion temperature raises by about 10% to above 2 keV, the electron temperature drops after termination of the ECRH to values $\approx 20\%$ below T_i . The orbit losses related to the neutral beam injection are discussed in Ref. [27].

18 **4. Stellarator Optimization**
19
20

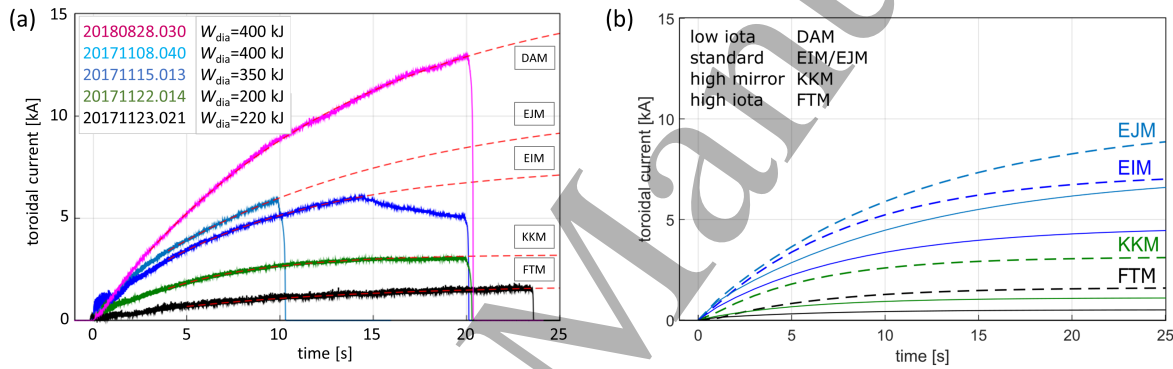
It is the ultimate goal of Wendelstein 7-X to demonstrate the beneficial effect of the optimized magnetic field geometry, in particular reduced neoclassical transport and bootstrap current along with magnetic islands well-localized at the edge and good magneto-hydrodynamic stability [4]. Fast particle confinement is another important aspect of optimization [31]. The sum of all should result in improved plasma confinement and fully integrated, stable plasma scenarios with simultaneously high $T_i \approx T_e$ at high particle densities. In the ion root regime [32], the energy confinement times τ_E are expected to be better than the ISS04 [33] stellarator scaling if most of the energy transport is neoclassical. High-performance plasma scenarios require good control of the plasma-wall interaction (in particular the impurity source), the heat and particle exhaust as well as the particle recycling. Details are discussed in Ref. [30]. In this section we present a number of experimental results that provide evidence for successful stellarator optimization.

Fig. 5(a) shows Rogowski coil measurements of the time evolution of the net toroidal plasma current for plasmas with constant ECR heating power in different magnetic field configurations: low iota (magenta line, label DAM), standard (blue lines, labels EIM and EJM), high mirror (green lines, label KKM), high iota (black lines, label FTM). The dashed red lines are exponential fits of the measurements. A prediction based on one-dimensional transport modelling and numerical calculation of the bootstrap current is shown in Fig. 5(b). The transport code requires as input the measured n_e and T_e profiles (not available for DAM). The time scale, mainly given by the R/L time ≈ 10 s (L and R are plasma inductance and resistance, respectively), and the expected strong reduction of the bootstrap current in high-mirror and high-iota configurations are well confirmed by both measurement and simulation. The simulations underestimate the measurements systematically (Fig. 5(b) solid lines). This might well be due to an (unintended) ECCD component, which is currently under investigation. By considering in the simulations reasonable residual ECCD of about 2 – 3 kA they quantitatively agree well with the measurements (Fig. 5(b) dashed lines). First findings on the reduction of the bootstrap current owing to magnetic field optimization were already reported from the previous operation campaign without divertor [19].

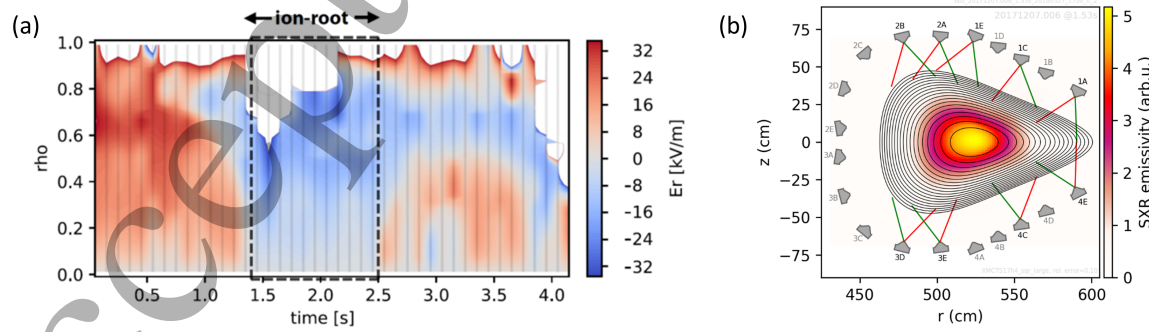
1
2 Overview of first Wendelstein 7-X high-performance operation 13
3
4
5
6
7
8
9
10
11
12
13

14 The long discharge duration enables to make use of electron cyclotron current drive
15 (ECCD) for a feed-forward control of the (edge) rotational transform [27, 28, 29], which
16 is changed by the toroidal current evolution that strongly depends on the magnetic
17 configuration and the discharge parameters. Central co-/counter ECCD leads under
18 certain discharge conditions to fast, repetitive electron temperature collapses in the
19 core or even a total plasma collapse. This is likely due to the rotational transform
20 crossing unity $\iota/2\pi = 1$, triggering an MHD instability [27, 29].
21
22

23 During the above discussed high density, high performance 1.1 MJ discharge with
24 pellet injection into a helium target plasma (cf. Sec.3), electrons and ions thermalize and
25 the ambipolar radial electric field E_r is expected to be negative throughout the plasma
26
27
28
29
30
31
32



33 **Figure 5.** (a) Time evolution of the toroidal current measured with Rogowski coils.
34 The different colors indicate the different magnetic configurations (see text). The
35 dashed lines are exponential best-fits to the decaying shielding current. (b) Transport
36 code simulations of the toroidal current based on experimental density and temperature
37 profiles for the same magnetic configurations. Solid or dashed lines indicate simulation
38 results without or with (unintended) residual ECCD, respectively: EJM 2.6 kA, EIM
39 2.7 kA, KKM 2.1 kA, FTM 1.8 kA.
40
41



54 **Figure 6.** (a) Radial electric field measured with the X-ray imaging camera system.
55 In the time interval $t = 1.5 \dots 2.5$ s a negative radial electric field forms throughout
56 the entire plasma core. (b) Tomographic reconstruction of the soft X-ray radiation in
57 the triangular plane, overlayed with the corresponding numerical plasma equilibrium
58 calculation (VMC). The X-ray cameras used for the reconstruction are indicated with
59 their viewing lines.
60

1
2 Overview of first Wendelstein 7-X high-performance operation 14
3
4
5
6
7
8
9
10

core (ion-root) [32]. This is clearly seen in measurements with the X-ray imaging crystal spectrometer (XICS, Fig. 6(a)), where the sudden transition from positive to negative E_r is correlated with the time interval during which $T_e \simeq T_i$. The neoclassical heat transport is predicted to be significantly reduced in the ion-root regime, as discussed more comprehensively in Ref. [34].

Fig. 6(b) shows the tomographic reconstruction of the soft X-ray radiation at the triangular cross section, using a set of poloidally arranged X-ray cameras [35]. The measurement is overlayed with the numerically calculated plasma equilibrium using the VMEC code [36] for $\langle\beta\rangle = 1\%$. There is a good agreement between measured and calculated plasma equilibrium. The Shafranov shift is found to be 1 – 2 cm only, as predicted for the optimized stellarator magnetic field with reduced Pfirsch-Schlüter current. For $\langle\beta\rangle \leq 1.5\%$ the plasma in Wendelstein 7-X is expected to be MHD stable [3, 4] and indeed no distinct activity is observed in the magnetic and X-ray diagnostics. As mentioned above, MHD instabilities can be driven by central ECCD. Alfvén modes were observed under certain NBI discharge scenarios. The analysis of the corresponding data is in progress and will be published elsewhere.

Impurity transport is another key issue of (optimized) stellarators. As discussed in Sec. 3 the radiative density limit strongly depends on the impurity concentration fraction. Furthermore, impurity accumulation is considered as a major stellarator issue, since in particular in the ion-root confinement regime with $T_e \simeq T_i$, the neoclassical impurity convection is inwards-directed, as for example observed in the predecessor device Wendelstein 7-AS [37, 38]. Recent neoclassical transport investigations have demonstrated that temperature screening can arise in stellarator plasmas in a mixed collisionality regime (for hydrogen and impurity ions) at high ion temperatures [39]. Up to now, at $\langle\beta\rangle \leq 1.5\%$, in Wendelstein 7-X no evidence for impurity accumulation

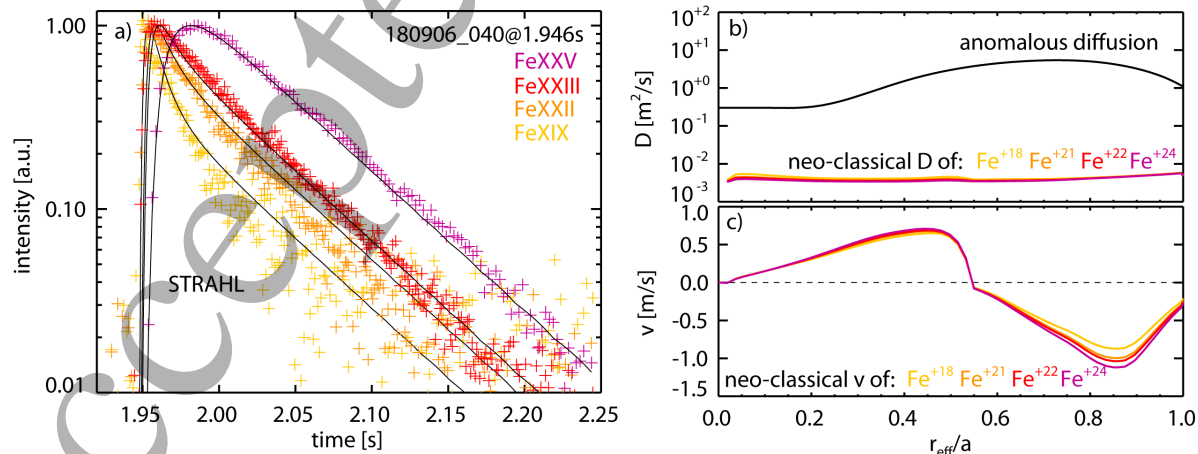
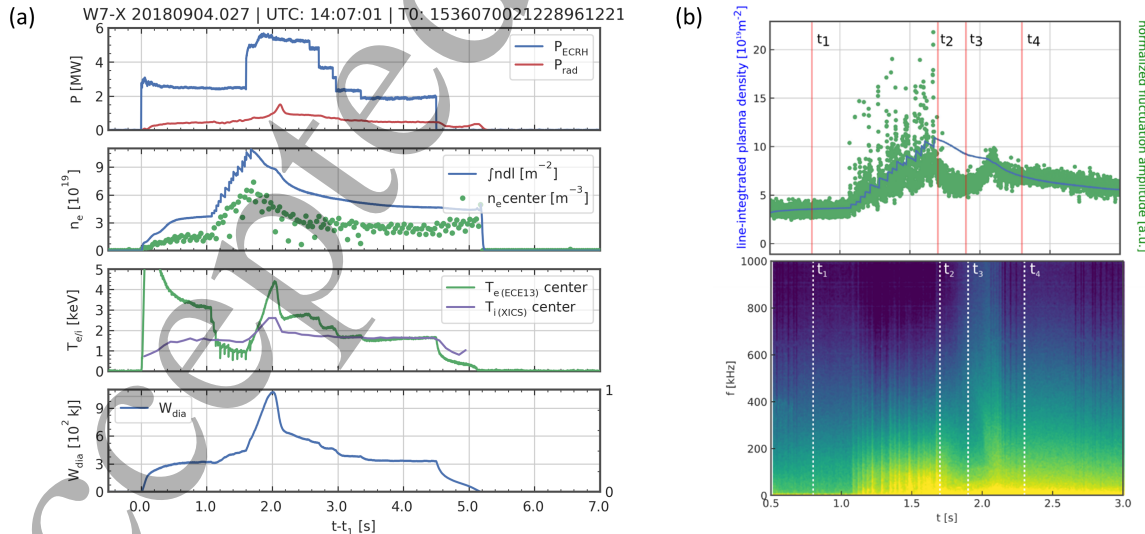


Figure 7. Laser blow-off injection of iron impurities into ECR heated hydrogen plasma. (a) Time evolution of selected iron ionization levels and forward-modelling curves (black lines). (b) Neoclassical and anomalous diffusion coefficient profiles. (c) Neoclassical convection velocity profiles.

1
2 *Overview of first Wendelstein 7-X high-performance operation* 15
3
4
5
6
7
8
9
10
11
12
13
14
15
16
17
18
19
20
21
22
23
24
25
26
27
28
29
30
31
32
33

has been found in all relevant plasma scenarios, even at high particle densities in the $1 \times 10^{20} \text{ m}^{-3}$ range as well as in the ion-root confinement regime. To investigate the transport physics of impurity particles, active diagnostics namely laser blow-off (LBO) [40] and impurity pellet injection [41] (tracer encapsulated solid pellets, TESPEL) are used, combined with fast high-resolution spectrometers. Fig. 7a shows the evolution of line radiation from different Fe ionization stages after injecting iron (LBO) into a hydrogen plasma at 5 MW of ECR heating power and a line-averaged plasma density of $2 \times 10^{19} \text{ m}^{-3}$. The rise-time and the decay-time of the different charge stages depend on the radial diffusion $D(r)$ and convection $v(r)$ profiles and consequently contain valuable information on the impurity transport. The measured data is compared with forward-modelling using the 1d impurity transport code STRAHL [42]. If as input parameters purely neo-classical diffusion and convection profiles are used, obtained from DKES [43] code runs [Fig. 7(b) and (c)], only poor agreement is obtained (not shown). In contrast to that, if additional anomalous diffusion is assumed [black line in Fig. 7(b)], the forward-modelling calculations match the experimental data very well [black curves in Fig. 7(a)]. The corresponding level of anomalous diffusion is more than two orders of magnitude above the neo-classical level, which strongly suggests dominant turbulent transport. Probably ion temperature gradient (ITG) driven turbulence is the main contributor here, since ITG is expected during flat density gradients and high T_e/T_i ratios as present during the experiments [44]. More detailed and systematic studies under different plasma parameters, as well as comparisons with gyro-kinetic simulations, are ongoing [45].



54 **Figure 8.** (a) High performance discharge with pellet injection during $t = 1 \dots 1.6 \text{ s}$
55 in a hydrogen target plasma. At $t = 1.6 \text{ s}$ the ECR heating power is doubled. The
56 diamagnetic energy peaks at $t \approx 2 \text{ s}$. (b) Temporal evolution of the line-integrated
57 plasma density (blue) and the turbulent density fluctuation level (green) for a pellet-
58 fueled discharge and the related spectrogram of plasma density fluctuations.
59
60

1
2 *Overview of first Wendelstein 7-X high-performance operation*

16

3
4
5
6
7
8
9
10
11
12
13
14
15
16
17
18
19
20
21
22
23
24
25
26
27
28
29
30
31
32
33
34
35
36
37
38
39
40
41
42
43
44
45
46
47
48
49
50
51
52
53
54
55
56
57
58
59
60
Wendelstein 7-X is neoclassically optimized and turbulent transport is expected to play a significant role in the regulation of radial heat diffusivity and particle exhaust. Turbulence studies are therefore of key importance and a suite of diagnostic instruments is available, namely correlation reflectometry [18], various probes for edge turbulence measurements [46] and phase contrast imaging (PCI) for characterization of turbulence in the plasma core [47]. PCI samples plasma density fluctuations along the line-of-sight of an infrared laser beam in the predominantly unfavorable magnetic curvature region. Nonlinear gyrokinetic simulations indicate that ion temperature gradient (ITG) and trapped electron modes (TEM) are possible in the plasma core but the latter are different from their tokamak counterparts [48, 49]. Both modes are unstable in regions of unfavorable magnetic curvature, which in Wendelstein 7-X are mainly localized in the outboard bean-shaped cross section. In usual gas-fueled discharges, ion temperature and plasma density gradient regions are well separated. Thus, ITG modes are destabilized deep in the plasma core, whereas TEM modes are localized in the edge plasma. An interesting observation is made with PCI when the plasma is centrally fueled by pellets (Fig. 8(a)). The density fluctuation amplitude is usually proportional to the line-integrated plasma density (Fig. 8(b)). However, after pellet fueling $t_2 = 1.6$ s, the fluctuation level suddenly drops and improved energy confinement is observed. The fluctuation spectrogram supports the picture: The entire fluctuation spectrum is temporarily reduced in amplitude, but evolves transiently for $t_3 < t < t_4$ starting from high frequencies until the usual linear scaling is recovered. Linear gyrokinetic simulations suggest [50], that the turbulence suppression is the result of a radial overlap between plasma density and temperature gradients, as it is generally observed in pellet discharges. Low T_e/T_i ratios and gradient length $L_{T_i} \simeq L_n \simeq 2 - 3$ m stabilize ITG, whereas TEM is naturally stabilized by the good magnetic curvature regions [48, 49]. This observation shows that indeed turbulent transport plays an important role in Wendelstein 7-X and that its reduction, e.g., by centrally peaked density profiles, could well be the key for the development of improved confinement scenarios. A more comprehensive discussion of turbulence and the related transport is found in Ref. [51].

44
45 **5. Summary**

46
47
48
49
50
51
52
53
54
55
56
57
58
59
60
In conclusion the plasma performance of the optimized stellarator Wendelstein 7-X has significantly improved after the installation of the graphite island divertor and the graphite wall elements. Impurity and heat exhaust are now well under control and long high-density discharges became accessible, especially after boronization. With a boronized wall, the radiative density limit could be shifted to three times higher values, on the expense of a slight degradation of the energy confinement time at the limit. With quite low ECR heating power, record values for the triple product in stellarators were achieved, albeit only transiently for a short time. The long discharges may well have set other records in comparison to other fusion research devices. The main limitations for high-performance long-pulse plasmas are limited heating power

1
2 *Overview of first Wendelstein 7-X high-performance operation* 17
3
4
5
6
7
8
9
10
11
12

and not yet fully implemented water cooling of the in-vessel components. Nevertheless, in general excellent plasma performance with up to $\langle \beta \rangle = 1.2\%$ and $\beta(0) = 3.5\%$ was achieved by relatively modest ECR O-mode heating power. More heating power is needed to explore the high beta $\langle \beta \rangle > \leq 5\%$ and low $\nu^* = 10^{-6} \dots 10^{-5}$ regimes, where stellarator optimization is relevant in all aspects.

12 **Acknowledgments**
13
14

This work has been carried out within the framework of the EUROfusion Consortium and has received funding from the Euratom research and training program 2014-2018 and 2019-2020 under grant agreement No 633053. The views and opinions expressed herein do not necessarily reflect those of the European Commision.
20
21
22

23 **References**
24
25
26
27
28
29
30
31
32
33
34
35
36
37
38
39
40
41
42
43
44
45
46
47
48
49
50
51
52
53
54
55
56
57
58
59
60

- [1] Boozer A., Phys. Plasmas **16**, (2009) 058102
- [2] Nührenberg J. and Zille R., Phys. Lett. **A 114**, (1986) 129
- [3] Grieger, G. et al., Phys. Fluids **B 4**, (1992) 2081
- [4] Beidler C. et al., Fusion Sci. Technol. **17**, 148-168 (1990)
- [5] Klinger T. et al, Plasma Phys. Controlled Fusion **59**(1) 014018 (2017)
- [6] Pedersen T.S. et al., Phys. Plasmas **24**, 055503 (2017)
- [7] Wolf R.C. et al., Nuclear Fusion **57**, 102020 (2017)
- [8] Klinger T. in Magnetic fusion energy: From Experiments to Power Plants, G. Neilson ed., Woodhead Publishing (2016)
- [9] Klinger T. et al., Fusion Eng. and Design **88**, 461465 (2013)
- [10] Renner H. et al., Plasma Phys. Controlled Fusion **44**(6) 1005-1019 (2002)
- [11] Bosch H.S. et al., Nuclear Fusion **52**(12) 126001 (2013)
- [12] Nagel M. et al., Fusion Eng. Design **86**(9-11) 1830-1833 (2011)
- [13] Erckmann V. et al., Fusion Science and Technol. **52** (2007) 291-312
- [14] Warmer F. et al., Plasma Phys. Control. Fusion **58** 074006 (2016)
- [15] McNeely P. et al., Fusion. Eng. Design **88**(6-8) 1034-1037 (2013)
- [16] Ongena J. et al., "Preparing the ICRH System for the Wendelstein 7-X Stellarator". Preprint: 2018 IAEA Fusion Energy Conference, Ahmedabad EX/P8-27
- [17] Yokoyama M. et al., Nuclear Fusion **47** 1213-1219 (2007)
- [18] Windisch T. et al., Plasma Phys. Controlled Fusion **59**(10) 105002 (2017)
- [19] Dinklage A. et al., Nature Physics **14** 855-860 (2018)
- [20] Wauters T. et al., Nuclear Fusion **58**(6) 066013 (2018)
- [21] Bozhenkov S. et al., "High density and high performance operation with pellet injection in W7-X". Preprint: 2018 IAEA Fusion Energy Conference, Ahmedabad EX/P8-8
- [22] Pedersen T.S. et al., Plasma Phys. Controlled Fusion **61** 014037 (2019)
- [23] Brakel R. et al., "Strategy and Optimization of Wall Conditioning at the Wendelstein 7-X Stellarator". Preprint: 2018 IAEA Fusion Energy Conference, Ahmedabad EX/P8-17
- [24] Fuchert G. et al., "Increasing the Density in W7-X: Benefits and Limitations". Preprint: 2018 IAEA Fusion Energy Conference, Ahmedabad EX/3-5
- [25] Zanca, P. et al., Nucl. Fusion **57**(5) 056010 (2017)
- [26] Winter, J. et al., J. Nucl. Mater. **14** 76177 (1990)
- [27] Wolf R. et al., to be submitted to Phys. Plasmas (2019)
- [28] Stange T. et al., submitted to Phys. Rev. Lett. (2018)

1
2 *Overview of first Wendelstein 7-X high-performance operation* 18
3
4

- 5 [29] Laqua H. P. et al., to be submitted to Nuclear Fusion (2019)
6 [30] Pedersen T.S. et al., "First Divertor Physics Studies in Wendelstein 7-X". Preprint: 2018 IAEA
7 Fusion Energy Conference, Ahmedabad EX/9-1
8 [31] Drevlak M. et al., Nuclear Fusion **54**(7) 073002 (2014)
9 [32] Helander P. et al., Plasma Phys. Control. Fusion **54** 124009 (2012)
10 [33] Yamada H. et al., Nuclear Fusion **45**(12) 1684-1693 (2005)
11 [34] Pablant N. et al., "Investigations of the Role of Neoclassical Transport in Ion-Root Plasmas on
12 W7-X". Preprint: 2018 IAEA Fusion Energy Conference, Ahmedabad EX/P8-31
13 [35] Brandt, C. et al., Fusion Eng. Design **123**, 887 (2017)
14 [36] Hirshman S. P. and Whitson J. C., Phys. Fluids **26**, 3553 (1983)
15 [37] Giannone L. et al., Plasma Phys. Contr. Fusion **42**(6) 603-627 (2000)
16 [38] Burhenn R. et al., Nuclear Fusion **49**(6) 065005 (2009)
17 [39] Helander P. et al., Phys. Rev. Lett. **118** 155002 (2017)
18 [40] Wegner T. et al., Rev. Sci. Instrum. **89**(7) 073505 (2018)
19 [41] Bussiahn R. et al., Rev. Sci. Instrum. **89** 10K112 (2018)
20 [42] Behringer, K. et al., Plasma Phys. Fusion Technol. **19** 57 (1987)
21 [43] Hirshman S. P. et al., Phys. Fluids **29** 2951 (1986)
22 [44] Geiger B. et al., accepted by Nuclear Fusion (2019)
23 [45] Wegner T. et al., to be submitted (2019)
24 [46] Killer C. et al., "Characterization of the W7-X Scrape-Off Layer Using the Multipurpose
25 Manipulator". Preprint: 2018 IAEA Fusion Energy Conference, Ahmedabad EX/P8-18
26 [47] Edlund E. et al., Rev. Sci. Instrum. **89** 10E105 (2018)
27 [48] Proll J. et al., Phys. Rev. Lett. **108**(24) 245002 (2013)
28 [49] Plunk G. et al., J. Plasma Phys. **83**, 715830404 (2017)
29 [50] Alcusion J. et al., to be submitted (2019)
30 [51] Grulke O. et al., "Plasma Dynamics and Transport Studies in Wendelstein 7-X". Preprint: 2018
31 IAEA Fusion Energy Conference, Ahmedabad EX/P8-9
32
33

34
35
36
37
38
39
40
41
42
43
44
45
46
47
48
49
50
51
52
53
54
55
56
57
58
59
60

Accepted